







First-order structural phase transition at low temperature in GaPt₅P and its rapid enhancement with pressure

A. Sapkota ^{1,2}, T. J. Slade,^{1,2} S. Huyan,^{1,2} N. K. Nepal ¹, J. M. Wilde,^{1,2} N. Furukawa ^{1,2}, S. H. Lapidus,³ L.-L. Wang ¹, S. L. Bud'ko ^{1,2} and P. C. Canfield ^{1,2}

¹*Ames National Laboratory, U.S. DOE, Iowa State University, Ames, Iowa 50011, USA*

²*Department of Physics and Astronomy, Iowa State University, Ames, Iowa 50011, USA*

³*X-ray Science Division, Advanced Photon Source, Argonne National Laboratory, 9700 South Cass Avenue, Lemont, Illinois 60439, USA*



(Received 7 June 2024; accepted 8 July 2024; published 25 July 2024)

Single crystals of XPt_5P ($X = \text{Al, Ga, and In}$), belonging to the 1-5-1 family of compounds, were grown from a Pt-P solution at high temperatures, and measurements of the ambient pressure, temperature-dependent magnetization, resistivity, and x-ray diffraction were made. Additionally, the ambient-pressure Hall resistivity and temperature-dependent resistance under pressure were measured on GaPt₅P. All three compounds have a tetragonal $P4/mmm$ crystal structure at room temperature with metallic transport and weak diamagnetism over the 2–300 K temperature range. Surprisingly, at ambient pressure, both the transport and magnetization measurements on GaPt₅P show a steplike feature in the 70–90 K region, suggesting a possible structural phase transition. Neither AlPt₅P nor InPt₅P have any signatures of a phase transition in their temperature-dependent electrical resistance and magnetization data. Both the hysteretic nature and sharpness of the features in the GaPt₅P data suggest that the transition is first-order. Single-crystal x-ray diffraction measurements provided further details of the structural transition with a possibility of a crystal symmetry different from $P4/mmm$ below the transition temperature. The transition is characterized by anisotropic changes in the lattice parameters and a volume collapse with respect to the high-temperature tetragonal crystal structure. Furthermore, satellite peaks are observed at two distinct and nonequivalent wave vectors (0, 0, 0.5) and (0.5, 0.5, 0.5), and density functional theory calculations present phonon softening, especially at (0.5, 0.5, 0.5), as a possible driving mechanism. Additionally, we find that the structural transition temperature increases rapidly with increasing pressure, reaching room temperature by ~ 2.2 GPa, highlighting the high degree of pressure sensitivity of GaPt₅P and fragile nature of its room-temperature structure. Even though the volume collapse and extreme pressure sensitivity suggest chemical pressure should drive a similar structural change in AlPt₅P, where both unit-cell dimensions and volume are smaller, its structure is found to be the same as that of the room-temperature GaPt₅P. Overall, GaPt₅P stands out as a sole member of the 1-5-1 family of compounds for which a temperature-driven structural change has been observed.

DOI: [10.1103/PhysRevB.110.024112](https://doi.org/10.1103/PhysRevB.110.024112)

I. INTRODUCTION

Recent discoveries of diverse and novel magnetic properties in $TM(\text{Pt/Pd})_5P$ ($TM = 3d$ transition metals) [1–6], which can be easily tuned with chemical doping, have renewed interest in the 1-5-1 family of compounds. The 1-5-1 family of compounds, XT_5Pn ($X =$ transition metals, main group elements; $T = \text{Pd, Pt}$; $Pn = \text{P, As}$), were first reported in 1970 [7], and the initial powder x-ray diffraction (XRD) measurements on some members determined that they crystallize in a tetragonal structure with the space group $P4/mmm$. The tetragonal structure is characterized by the Pt and/or Pd atoms at $4i$ and $1a$, X atoms at $1c$, and Pn at $1b$ Wyckoff positions, and it is a layered structure with XPt_{12} polyhedral layers separated along the c -axis by an Pn layer.

Despite having the same tetragonal $P4/mmm$ crystal structure, the TM 1-5-1 compounds exhibit a diverse magnetism, from ferromagnetism (FM) to antiferromagnetism (AFM) and with local to itinerant characters [1–6,8]. In particular,

MnPt₅As [1] ($T_C \approx 280$ K) and $\text{Cr}_{1+x}\text{Pt}_{5-x}\text{P}$ [5] ($T_C \approx 464$ K) exhibit ferromagnetic ordering, whereas MnPt₅P [2] ($T_N \approx 190$ K) and FePt₅P [8] (multiple transitions between 70 and 90 K) order antiferromagnetically. Among these, $\text{Cr}_{1+x}\text{Pt}_{5-x}\text{P}$ and FePt₅P are itinerant, whereas MnPt₅P is local-moment-like. Also, isovalent doping of MnPt₅P with Pd, as detailed in Ref. [6], results in a magnetic phase diagram characterized by multiple magnetic states and exemplifies chemical substitution as an effective tuning parameter of their physical properties.

Furthermore, the presence of a large amount of Pt or Pd can provide enhanced density of states at the Fermi surface and large spin-orbit coupling, indicating a possibility of large, non-rare-earth-based magnetocrystalline anisotropy. Overall, the XT_5Pn family of compounds offers a rich space to study the interplay between ferromagnetism, antiferromagnetism, potential topological properties [4], and possibly other structural and electronic phases [9]. To better understand the diverse properties exhibited by the $3d$ transition metal containing XPt_5P compounds, it is useful

to provide a comparison with analogs in which X is not moment-bearing.

In this regard, 3A element (Al, Ga, In, Tl) XPt_5P members are ideal candidates as they do not have any moment-bearing atoms, and they can be regarded as nonmagnetic analogs of the $TM(Pt/Pd)_5Pn$ compounds. Other than the first report of their structure in Ref. [7], only a few studies of some members of 3A element XPt_5P exist, and the studies are mostly limited to room temperature. For instance, powder XRD data on $InPt_5P$ in Ref. [10] confirmed its room-temperature crystal structure to be tetragonal with space group $P4/mmm$. Density functional theory (DFT) calculations predicted it to be metallic and diamagnetic, which was also confirmed by the magnetic measurements in the temperature range of 4–300 K.

Here, we present temperature dependence studies investigating the physical properties of three XPt_5P ($X = Al, Ga,$ and In) compounds with the main focus on $GaPt_5P$, due to an observed anomaly. Our powder x-ray diffraction results demonstrate that, similar to the earlier reports on XT_5Pn members, the room-temperature crystal structure of all three compounds is tetragonal with $P4/mmm$ crystal symmetry. Furthermore, the temperature-dependent electrical resistance and magnetic susceptibility of single crystalline $AlPt_5P$ and $InPt_5P$ show metallic resistance versus temperature curves and weakly diamagnetic behavior (suggesting rather broad bands, or a low density of states at the Fermi surface). No features suggesting any sort of phase transition exist in these data over the temperature range of 300–2 K. On the other hand, in addition to metallicity and diamagnetism, $GaPt_5P$ has a sharp and clear anomaly in both the electrical resistance and magnetic susceptibility in the 70–90 K temperature range (depending upon the specific measurement as well as the direction of temperature change), indicating a possible structural change. To better understand the anomaly, additional measurements, such as single-crystal x-ray diffraction, Hall resistivity, and high-pressure resistance measurements, were carried out on $GaPt_5P$ single crystals.

Our single-crystal x-ray diffraction measurements on $GaPt_5P$ confirm the first-order structural transition with anisotropic changes in lattice parameters, and a volume collapse with respect to the high-temperature tetragonal structure. The observed satellite peaks suggest a crystal symmetry with an enlarged unit cell, where $a' = b' = \sqrt{2}a$ and $c' = 2c$, agreeing with the predictions from our DFT calculations. Furthermore, hysteresis, associated with the first-order structural transition, is apparent in all the measurements. The low-temperature structure of $GaPt_5P$ is categorized as a double- Q type structure with respect to $P4/mmm$, as evidenced by the presence of satellite peaks with two distinct wave vectors. DFT calculations present phonon softening as a possible mechanism for the transition.

In addition, we find that the structural phase transition in $GaPt_5P$ is remarkably pressure-sensitive, as the resistive feature associated with it shifts towards higher temperature with increasing pressure, bringing it to ~ 300 K by 2.2 GPa. Given that the structural phase-transition temperature crosses the pressure medium solidification line, $GaPt_5P$ offers a case study of the effects of pressure medium hydrostaticity on a structural phase transition.

II. EXPERIMENTAL DETAILS AND COMPUTATIONAL METHODS

A. Crystal growth

Single crystals of XPt_5P ($X = Al, Ga, In$) were grown from a ternary X -Pt-P solution analogous to that used to produce other MPt_5P phases ($M = Cr, Mn, Fe$) [4,5]. The starting materials were elemental Pt powder (Engelhard, 99+% purity), chips of red P (Alpha Aesar, 99.99%), and Ga or Al or In (Alpha Aesar, 99.999%). The elements were weighed according to a nominal molar ratio of $X_9Pt_{71}P_{20}$ and contained in the bottom side of a three-piece alumina Canfield crucible set (CCS, sold by LSP Ceramics) [11,12]. The CCS was sealed in a fused silica ampule and was held in place with a small amount of silica wool, which serves as cushioning during the decanting step [13]. The ampules were evacuated three times and back-filled with $\sim 1/6$ atm Ar gas prior to sealing. Using a box furnace, the ampules were first warmed to 250 °C over 6 h, then to 1180 °C in an additional 8 h. After holding at 1180 °C for 6 h, the furnace was cooled to 830 °C in 72 h, and upon reaching the final temperature, the remaining liquid phase was decanted by inverting the ampules into a centrifuge with a specially made metal rotor and cups [13]. After cooling to room temperature, the ampule was cracked open to reveal clusters of thin, metallic, platelike crystals. Some of the representative single crystals of $GaPt_5P$ grown using this method are shown in Fig. 4(c) below, over a mm grid. Single crystals of $AlPt_5P$ and $InPt_5P$ were similar, although the $AlPt_5P$ crystals were not as well faceted.

B. Powder x-ray diffraction

The room-temperature crystal structures of the three XPt_5P compounds were confirmed from the refinement of the powder x-ray diffraction data measured at 11-BM beamline of the Advanced Photon Source at Argonne National Laboratory. Select single crystals of $AlPt_5P$, $GaPt_5P$, and $InPt_5P$ were ground with a mortar and pestle to a fine powder and passed through using a 40 μm mesh sieve. Each of the powders was loaded into a 11-BM Kapton capillary tube, and the diffraction patterns were collected using monochromatic x-ray radiation of wavelength of $\lambda = 0.4589$ Å from -6 to $28^\circ 2\theta$ with a step size of 0.001° and with a counting time of 0.1 s/step. Rietveld refinement using GSAS-II software [14] was performed to confirm the reported crystal structure.

C. High-resolution single-crystal x-ray diffraction

Single-crystal x-ray diffraction measurements were performed on an in-house four-circle diffractometer (Huber) using $Cu K\alpha 1$ radiation from a rotating anode x-ray source, using a germanium (1 1 1) monochromator. A He closed-cycle refrigerator was used for temperature-dependent measurements between 10 and 120 K. Three beryllium domes were used as a vacuum shroud, heat shield, and the last innermost dome containing the sample. The innermost dome was filled with a small amount of He gas to improve thermal contact to the sample surface. Measurements were carried out on single crystal of $GaPt_5P$ with mass ~ 0.025 g attached to a flat copper sample holder that is attached to the cold finger. Additionally, room-temperature measurements were carried on $AlPt_5P$ and

InPt₅P single crystals with masses of ~ 0.004 and ~ 0.002 g, respectively.

D. Magnetization and transport

Magnetization measurements were performed in a Quantum Design Magnetic Property Measurement System (QD MPMS-classic) SQUID magnetometer operating in the dc measurement mode. The magnetic measurements were conducted with the field oriented parallel and perpendicular to the c -axis, where c is perpendicular to the large surface of the platelike crystals [see Fig. 4(c) below]. For the $H \parallel c$ measurements, the sample was glued to a plastic disk, and background measurements using the empty disk were first measured and the values subtracted. For the $H \perp c$ measurements, the sample was held in place between two straws.

Resistance measurements were done with a Quantum Design Physical Property Measurement System (QD PPMS). The samples were prepared by cutting the crystals into rectangular bars, and the contacts were made by spot welding 25- μm -thick annealed Pt wire onto the samples in standard, linear four-point geometry so that the current was flowing within the ab -plane. To ensure good mechanical strength, a small amount of silver epoxy was painted over the spot-welded contacts, and the contact resistances were normally $\sim 1 \Omega$.

Hall resistivity was measured using a four-probe configuration with the applied field held perpendicular to the current direction. To account for small misalignment of the Hall voltage contacts, the odd component of the signal $\rho_H = \frac{\rho(+H) - \rho(-H)}{2}$ was taken as Hall resistivity. Here, $\rho(+H)$ and $\rho(-H)$ are the measured Hall resistivity values for positive and negative applied magnetic field, respectively. Electrical transport measurements were performed using an alternating current transport option of the QD PPMS.

E. Transport under pressure

The temperature-dependent electrical transport measurements down to 1.8 K and under pressures up to 2.2 GPa were carried out in our laboratory-made piston-cylinder pressure cell [15] that fits QD PPMS. A linear, four-terminal configuration was used for the arrangement of wires for contacts, with the applied current direction along the ab plane. High-purity lead (Pb) was used for the determination of pressure at low temperatures [16]. The mixed fluid with 4:6 of light mineral oil and n -pentane was used as the pressure-transmitting medium, which solidifies at room temperature in the pressure range of 3–4 GPa and has a well-determined $T(P)$ solidification line [17].

The GaPt₅P single crystal used for these measurements under pressure is different from those used for the ambient-pressure transport measurements discussed in the previous section.

F. Computational method

Density functional theory [18,19] (DFT) calculations were performed with PBEsol exchange-correlation functional including spin-orbit coupling (SOC) using a plane-wave basis set and projector augmented wave method [20], as

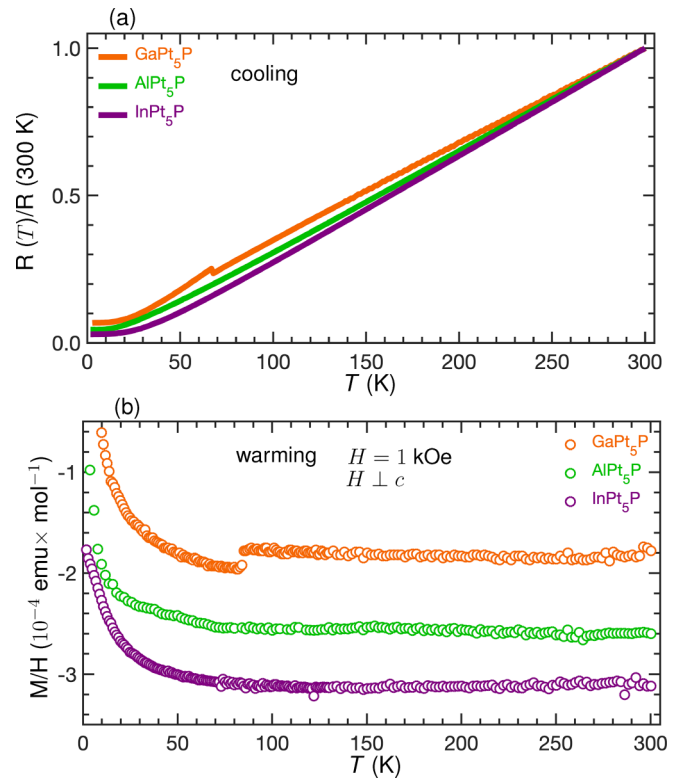


FIG. 1. Temperature dependence of (a) resistance R normalized to its 300 K value, and (b) susceptibility ($\chi = \frac{M}{H}$) for AlPt₅P, GaPt₅P, and InPt₅P. The measurements cover the temperature range of ~ 2 –300 K and include cooling data for the resistance and warming for magnetization.

implemented in the Vienna Ab-initio Simulation Package [21,22] (VASP). We used a kinetic energy cutoff of 319 eV, a Γ -centered Monkhorst-Pack [23] ($10 \times 10 \times 6$) k -point mesh, and a Gaussian smearing of 0.05 eV. The ionic positions and unit-cell vectors were fully relaxed with the remaining absolute force on each atom being less than 2×10^{-3} eV/Å. The DFT-calculated lattice parameters with PBEsol+SOC are within 1% of the experimental data. Phonon band dispersion of the GaPt₅P was calculated with the finite-difference method using PHONOPY [24].

III. RESULTS AND DISCUSSION

A. Transport and magnetic properties of $X\text{Pt}_5\text{P}$ ($X = \text{Al, Ga, In}$)

Figure 1 shows the temperature dependence of the normalized resistance (while cooling) and magnetic susceptibilities (while warming) for AlPt₅P, GaPt₅P, and InPt₅P. All three compounds exhibit metallic temperature dependence of the resistance and essentially temperature-independent magnetic susceptibilities (except for small, low-temperature Curie tails, to be discussed below), consistent with a low density of states at the Fermi surface. DFT calculations of the electronic structures of GaPt₅P, shown in Fig. 11 of Appendix A 1, indicate a small but nonzero density of states (DOS) at the Fermi level, and similar results were reported for InPt₅P in Ref. [10]. The main contribution at the Fermi level is due to the d -orbitals of the transition metal Pt.

The residual resistivity ratios $\text{RRR} = R(300 \text{ K})/R(2.0 \text{ K})$ are 20, 15, and 34 for AlPt_5P , GaPt_5P , and InPt_5P , respectively, and are consistent with well-ordered compounds. Overall, the magnetic susceptibilities display features typical of non-moment-bearing compounds with a small amount of paramagnetic (PM) impurity. To quantify the level of the PM impurities, we fit the low-temperature part ($<50 \text{ K}$) of the data using the Curie-Weiss law,

$$\chi = \frac{C}{T - T_c} + \chi_0, \quad (1)$$

where C is the Curie constant; $C = 0.002 \text{ emu K/mol}$ was obtained from our fit of the GaPt_5P data in Fig. 1(b). As discussed in Ref. [25], the value of the Curie constant C can be used to calculate the effective magnetic moment per formula unit (f.u.) using the relationship

$$\mu_{\text{eff}} = \sqrt{\frac{8C}{n}} \mu_B \text{ (cgs)}, \quad (2)$$

where n is the number of magnetic atoms per formula unit.

Next, to gauge the amount of the impurity, we assumed that the magnetic impurity present in our GaPt_5P sample is Mn^{2+} (this was just an assumption, not a known impurity), and it exists as $\text{Ga}_{1-n}\text{Mn}_n\text{Pt}_5\text{P}$, given that MnPt_5P is a known member of the 1-5-1 family. The spin-only effective moment of Mn with $S = 5/2$ and $g = 2$ can be calculated using

$$\mu_{\text{cal}}^{\text{Mn}} = g\sqrt{S(S+1)}\mu_B = 5.9\mu_B. \quad (3)$$

Replacing this value in Eq. (2) as μ_{eff} , we get $5.9\mu_B = \sqrt{\frac{8C}{n}}\mu_B$, and on solving this we get $n = 0.0005$, i.e., a very small amount of Mn impurity. Even for the smaller moment impurity with $S = 1/2$ and $g = 2$, the impurity concentration is still very small, $n = 0.005$. Overall, the implication of our calculation is that the amount of paramagnetic impurities (PMI) present in our sample, $\text{Ga}_{1-n}(\text{PMI})_n\text{Pt}_5\text{P}$, was infinitesimal. This low level of impurities, or disorder, is consistent with the relatively large RRR values we found above.

Also, the Curie-Weiss fits to the low-temperature part ($<50 \text{ K}$) of the $\frac{M}{H}$ data of AlPt_5P and InPt_5P , shown in Fig. 1(b), produce $C = 0.0007$ and 0.0028 emu K/mol , respectively. The values are comparable to that of GaPt_5P indicating an infinitesimal amount of PMI in these samples as well.

In addition to metallicity and diamagnetic behavior, GaPt_5P has a conspicuous, anomalous feature that is clearly visible as a sharp jump in both resistance and susceptibility data. The jump appears near 70 K in the resistance (cooling) data and near 84 K in the susceptibility (warming) data, suggesting a first-order phase transition with rather large hysteresis. Given that no such transitions exist for both $(\text{Al}/\text{In})\text{Pt}_5\text{P}$ and have not been reported for any of the known $X\text{Pt}_5\text{P}$ materials, we focus on exploring the feature in GaPt_5P for the rest of the paper.

B. Transport and magnetic properties of GaPt_5P : A first-order structural transition

Figure 2 shows the temperature dependence of the resistivity and magnetic susceptibility ($\chi = \frac{M}{H}$) for GaPt_5P only.

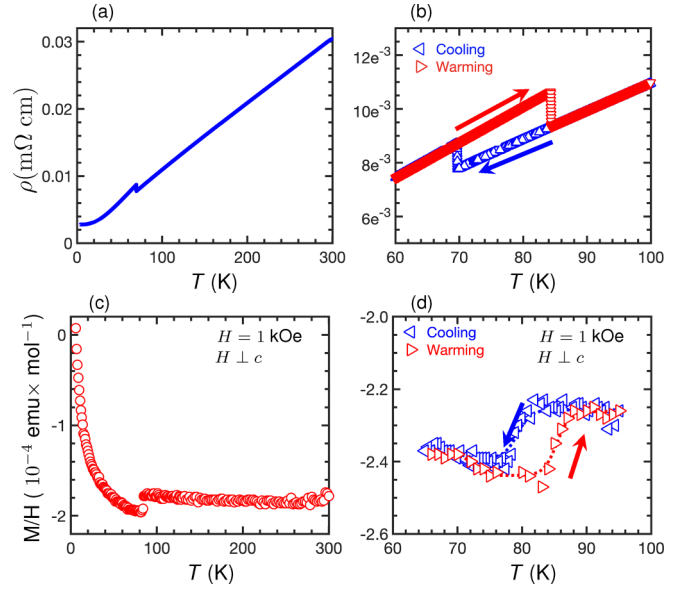


FIG. 2. Temperature dependence of resistivity and susceptibility ($\chi = \frac{M}{H}$) of GaPt_5P . Panels (a) and (c) show the measurements in the large temperature range up to 300 K and contain either cooling or warming data, respectively. Panels (b) and (d) show the results for both warming and cooling to highlight the hysteresis, and they contain data only around the anomalous jump or transition.

As discussed above, in addition to metallicity and diamagnetism, sharp and discontinuous changes are apparent in both measurements, and the onset for warming and cooling occurs at different temperature indicating the hysteresis. Onset here corresponds to the starting point of the discontinuity, and the values are different for warming and cooling measurements.

In the case of the resistivity, as shown in Fig. 2(b), the sharp, discontinuous increase appears upon cooling near 70 K, and the higher-temperature values are recovered on warming near 84 K. The hysteresis between warming and cooling profiles implies a first-order transition. Alteration to the electronic structure induced by a structural transition is the likely cause of the resistive anomaly. The temperature-dependent Hall data, shown in Fig. 3, indeed support this notion of a change in the electronic structure. Below $\approx 70 \text{ K}$, the Hall coefficient also changes abruptly from negative to positive,

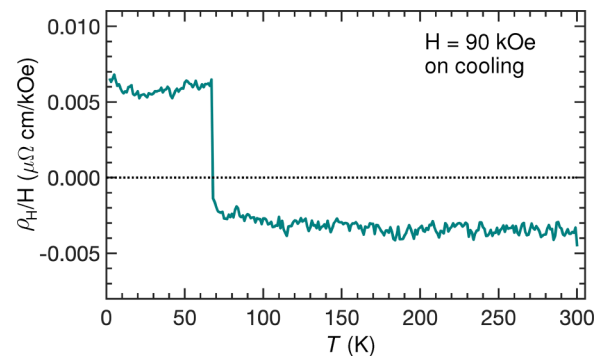


FIG. 3. Temperature dependence of the Hall coefficient (ρ_H/H) of GaPt_5P .

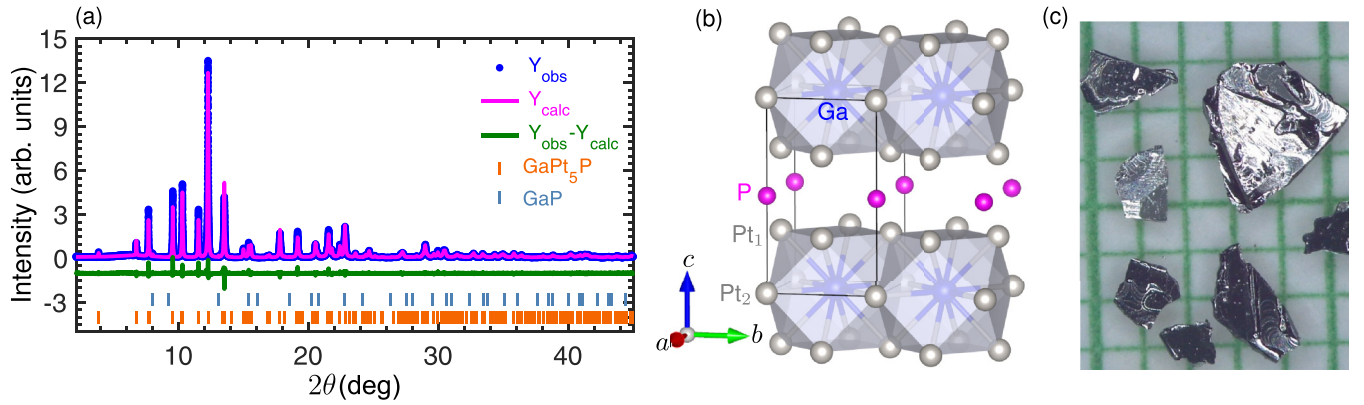


FIG. 4. (a) Rietveld refinement of the room-temperature synchrotron powder x-ray diffraction data of GaPt₅P with $R_{wp} = 9.87\%$, $R_p = 7.97\%$, and $GOF = 1.56$. Blue dots and magenta solid lines correspond to the data and calculated pattern, respectively. The green line and vertical orange markers are the difference between data and calculation and allowed Bragg reflections, respectively. (b) Crystal structure of GaPt₅P. (c) Pictures of solution grown GaPt₅P single crystals on a mm grid. The crystallographic c -axis is perpendicular to the platelike surfaces.

indicating that the dominant charge carrier changes from the electron to the hole type.

Like the resistivity curves, the hysteresis observed in the $\frac{M}{H}$ data, in Fig. 2(d), supports the idea that the transition is first-order. Also, we note that the width of the hysteresis between warming/cooling sweeps is slightly wider in the resistance measurement, which most likely reflects the faster warming-cooling (ramp) rate used for these measurements than for the magnetization. Moreover, the hysteresis width and transition temperatures exhibit history dependence in GaPt₅P. Variation in the hysteresis width and transition temperatures of GaPt₅P with both the ramp rate and in different cycles of the measurements is shown in Fig. 15 in the Appendix and discussed briefly in Appendix A 4.

The change in magnetization at the transition is consistent with the change in the Hall coefficient. The larger, diamagnetic signal, just below the transition [Figs. 2(c) and 2(d)], implies a decrease in the Pauli paramagnetism which itself would be associated with a decrease in DOS (E_F). Such a change is also implied by the Hall data, which have a smaller magnitude for temperatures just above the transition temperature and a larger magnitude just below. As such, the Hall data also imply a smaller DOS (E_F) for temperature below the transition temperature.

C. Powder x-ray diffraction: Room-temperature crystal structure

Before studying GaPt₅P structure upon cooling, it is important to more carefully examine its structure at room temperature and compare it to AlPt₅P and InPt₅P, especially considering the compelling evidence indicating a possible structural phase transition in GaPt₅P below room temperature.

Hence, to confirm the room-temperature crystal structure, our synchrotron powder x-ray diffraction data measured on GaPt₅P were refined using Rietveld analysis and GSAS-II software. In agreement with the previous reports [7], the room-temperature crystal structure of GaPt₅P is tetragonal

with space group $P4/mmm$. Room-temperature powder x-ray diffraction data and the final refinement plots are shown in Fig. 4(a). The crystal structure obtained from the refinement is shown in Fig. 4(b) and is isostructural to other XPt₅P compounds. It is a layered structure, comprising a cuboctahedron of a Ga-centered GaPt₁₂ layer separated along the c -axis by a P layer.

In addition to the main phase, a secondary phase of GaP exists in a small amount (<0.5 wt. %). Statistical parameters from the refinement including both phases in the model are $R_{wp} = 9.87\%$ and $GOF = 1.56$, indicating a reasonable refinement. The unit-cell parameters, atomic coordinates, and isotropic displacement parameters obtained from the refinement are summarized in Tables I and II. Refined parameters are similar to the ones reported earlier for GaPt₅P in Ref. [7].

Similar synchrotron powder x-ray measurements were also carried out on AlPt₅P and InPt₅P for comparison. Figure 5 shows the powder pattern for all three compounds along with their respective fits from the refinement with $P4/mmm$ crystal symmetry. R -factors and the goodness of fits, listed in the figure, obtained from all three refinements indicate a reasonable refinement, thereby confirming that the room-temperature crystal structure for all three (Al, Ga, In)Pt₅P compounds is indeed tetragonal with the space group $P4/mmm$. Refined lattice parameters for all three compounds are listed in Table III.

TABLE I. Unit-cell parameters at room temperature obtained from the Rietveld refinement.

Formula	GaPt ₅ P
space group	$P4/mmm$
a (Å)	3.90038(2)
c (Å)	6.85564(3)
α	90
β	90
γ	90
volume (Å ³)	104.2948(8)

TABLE II. Refined atomic coordinates and the equivalent isotropic displacement parameters of GaPt₅P at room temperature.

Atoms	Wyckoff	<i>x</i>	<i>y</i>	<i>z</i>	Occ.	<i>U</i> _{eq}
Pt1	4 <i>i</i>	0	0.5	0.28978(3)	1	0.0043(1)
Ga	1 <i>c</i>	0.5	0.5	0	1	0.0080(5)
P	1 <i>b</i>	0	0	0.5	1	0.0092(11)
Pt2	1 <i>a</i>	0	0	0	1	0.0045(2)

The lattice parameters and volume increase from Al to In, in accordance with the corresponding increase in atomic radii from Al to In.

Impurities or secondary phases identified in AlPt₅P, GaPt₅P, and InPt₅P samples from our powder diffraction measurements are binary AlP, GaP, and InP, respectively. All three of them are diamagnetic [26–29] as well as the Pt₂ [30] found in AlPt₅P. Hence, the paramagnetic impurities suggested from the susceptibility plots, in Fig. 1(b), and discussed above in Sec. III A are yet to be identified. The absence of the peaks corresponding to the paramagnetic impurities is due to their infinitesimal amount in the sample.

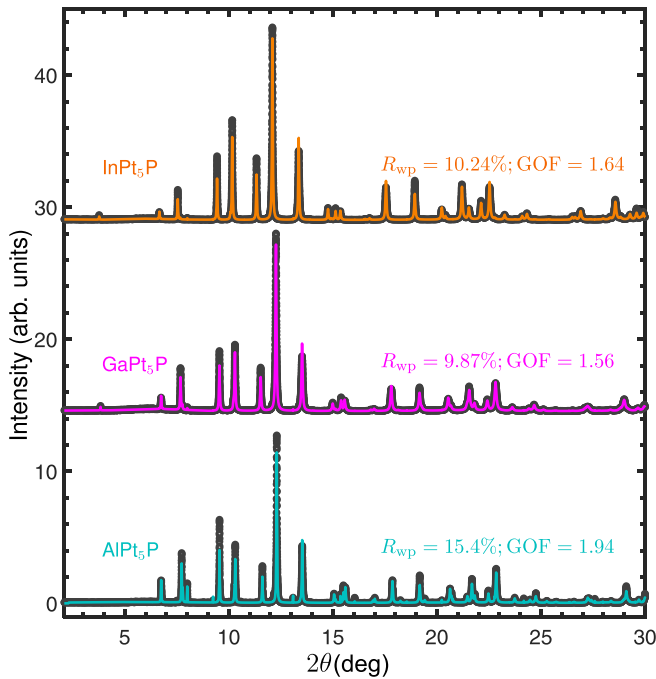


FIG. 5. Rietveld refinement of the room-temperature synchrotron powder x-ray diffraction data of XPt₅P X = Al, Ga, and In. Black dots and colored solid lines correspond to the data and calculated pattern, respectively. Corresponding *R*_{wp} and GOF are given alongside the figure with the same color as the calculated pattern. Small minority peaks corresponding to the binary compounds AlP, GaP, and InP were present in a small amount in all three powder patterns, respectively, but in the case of AlPt₅P additional impurity peaks corresponding to other binary, such as Pt₂, were also present. Measurements on all three powder samples were carried out with identical conditions as discussed in Sec. II B.

TABLE III. Refined lattice parameters and volume of AlPt₅P, GaPt₅P, and InPt₅P at room temperature.

	<i>a</i> (Å)	<i>c</i> (Å)	Volume (Å ³)
AlPt ₅ P	3.89832(1)	6.80627(3)	103.434(1)
GaPt ₅ P	3.90038(2)	6.85564(3)	104.295(1)
InPt ₅ P	3.94700(1)	6.97401(3)	108.647(1)

D. Single-crystal x-ray diffraction of GaPt₅P: Structural transition with a potential crystal symmetry change

To further determine the details of the structural transition in GaPt₅P, we performed high-resolution single-crystal x-ray diffraction measurements between 10 and 120 K. Various points in the reciprocal space (*H* 0 *L*) with respect to tetragonal *P4/mmm* crystal symmetry were measured, and to acquire the lattice parameters, (0, 0, 6) and (2, 0, 5) Bragg peaks were measured on warming and cooling. First, the (0 0 6) peak was measured in the ramp-mode with a rate of 0.1 K/min and the measurements of (2, 0, 5) peaks after with a rate of 0.15 K/min. The slow ramp rates minimize the temperature lag between the sensor and sample. Figure 6 shows the evolution of the (0, 0, 6) and (2, 0, 5) peaks while warming. Both peaks show a sudden shift in the peak positions upon warming through the mid-80 K's. At 82 K, a splitting of the (0, 0,

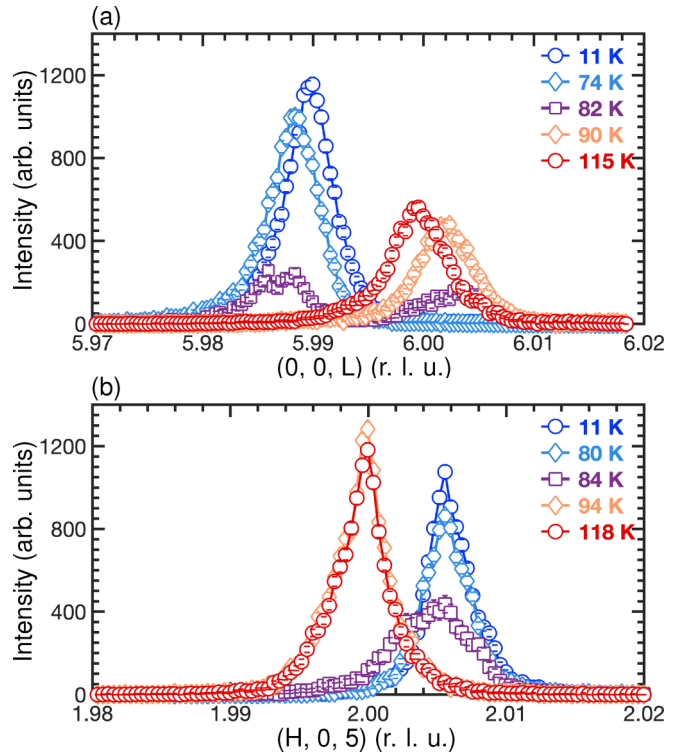


FIG. 6. (a) and (b) Evolution of the (0, 0, 6) and (2, 0, 5) Bragg peaks of GaPt₅P with temperature while warming. The shift in the peak positions away from the *L* = 6 in (a) and *H* = 2 in (b) corresponds to the change in the lattice parameters with temperature. The reciprocal space was defined with respect to the lattice parameters of high temperature, without updating the orientation matrix and length scales as the temperature changes.

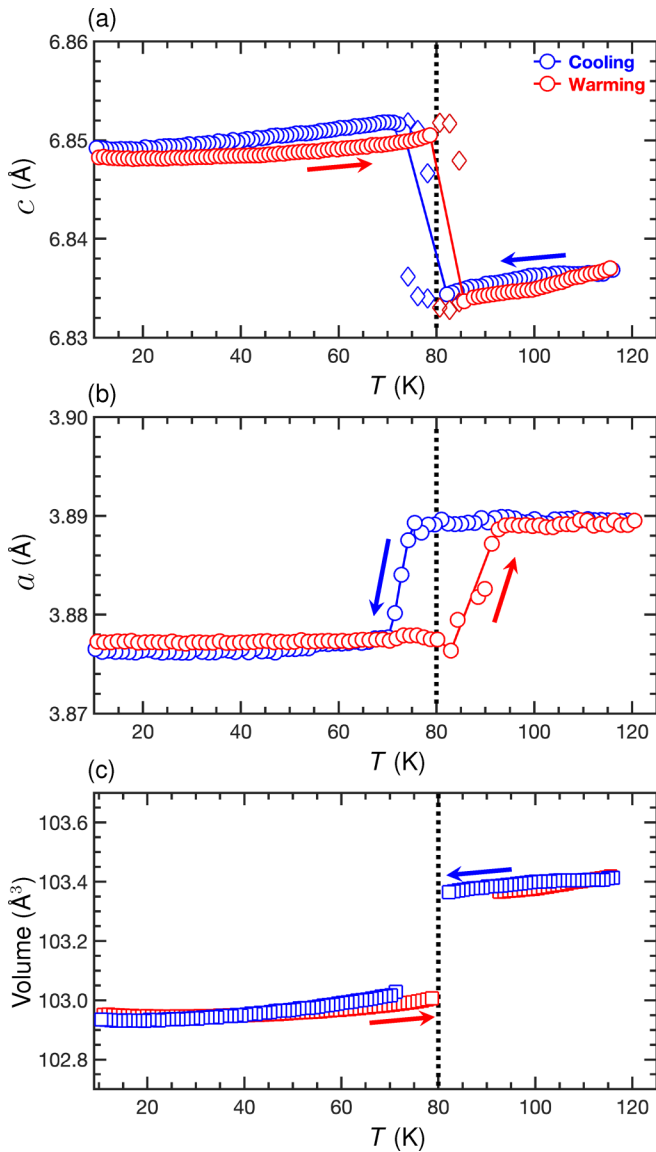


FIG. 7. Temperature dependence of the lattice parameters and volume, defined with respect to high-temperature tetragonal structure, while cooling and warming. Blue and red data correspond to measurements while cooling and warming, respectively. Diamond markers in (a) correspond to the coexistence region, hence the figure has two values. Solid blue and red lines in (a) and (b) connect the data points, excluding the coexistence regions, and provide a qualitative visualization of the hysteresis. Additionally, the dotted vertical line at ~ 80 K is the onset temperature, at least for the warming measurements, and roughly highlights the transition temperature T_s in our measurements.

6) peak is apparent, and at 84 K, a shoulder on the (2,0,5) peak is observed. These features indicate the coexistence of two phases and support the notion of the first-order structural transition.

Next, the lattice parameters of the tetragonal unit cell were obtained from the fits of the peaks in Fig. 6 with a pseudo-Voigt line shape. Consistent with the first-order transition, lattice parameters in Fig. 7 show abrupt and discontinuous changes along with clear thermal hysteresis. However, the

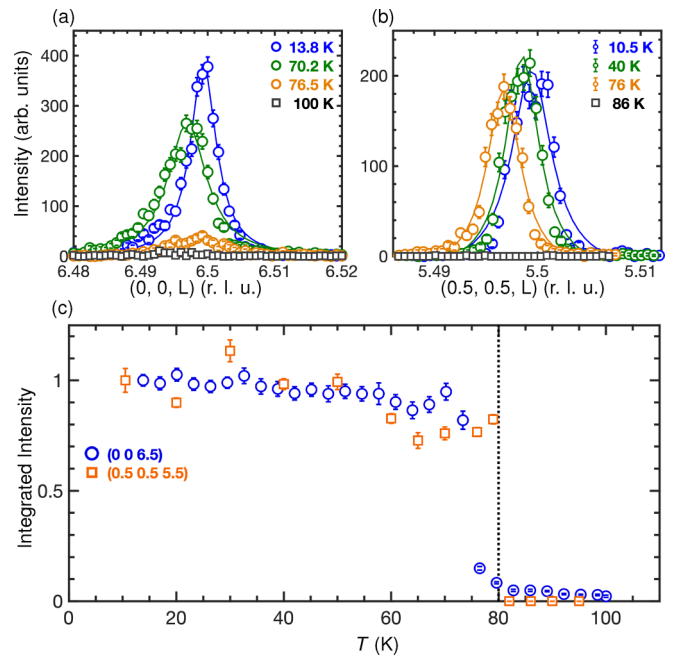


FIG. 8. X-ray diffraction measurements of the satellite peaks at wave vectors (a) $\tau = (0, 0, 0.5)$ and (b) $\tau = (0.5, 0.5, 0.5)$ with respect to the high-temperature $P4/mmm$ crystal symmetry. (a) $[0, 0, L]$ scans of the (0, 0, 6.5) Bragg peak on cooling illustrating its evolution. (b) Similar plots for the (0.5, 0.5, 5.5) Bragg peaks measured while warming. (c) Normalized integrated intensity of the (0, 0, 6.5) and (0.5, 0.5, 5.5) satellite peaks as an order parameter showing the discontinuity and phase transition below ≈ 80 K on warming (with a lower temperature discontinuity on cooling). The integrated intensities are normalized to the corresponding value at the base temperature and are obtained after fitting the plots in (a) and (b) with pseudo-Voigt line shapes.

changes in both lattice parameters are anisotropic: the c lattice parameter increases below the transition temperature, whereas the a lattice parameter decreases. For warming, the onset for the transition is $T_{\text{onset}} \sim 80$ K for both c and a lattice parameters but differs in the case of cooling. The temperature evolution of the volume obtained by using these lattice parameters, except in the coexistence region, is shown in Fig. 7(c), and upon cooling the unit-cell volume decreases by 0.33%. Hysteresis is apparent in each of the three figures, but the hysteresis width differs for c and a lattice parameters, Figs. 7(a) and 7(b), respectively. As shown in Fig. 15 in Appendix A 4, the difference most likely arises from the combination of different ramp rates and the measurements being done during different cycles.

In addition to the changes observed in the lattice parameters and nuclear Bragg peaks, satellite peaks at the commensurate wave vectors of $\tau = (0, 0, 0.5)$ and $(0.5, 0.5, 0.5)$ were observed below the transition. Figures 8(a) and 8(b) show the temperature evolution of the satellite peaks at wave vectors (0, 0, 6.5) and (0.5, 0.5, 5.5), respectively. Both figures clearly illustrate their appearance at lower temperature approximately below transition temperature T_s in Fig. 7. To further highlight this, integrated intensity from the fits of the peaks in (a) and (b) is shown in Fig. 8(c). Similar to the lattice parameters, we found that the forbidden satellite peaks appear

below $T_s \approx 80$ K (on warming) and also have a discontinuity or sharp onset. Furthermore, these superlattice peaks are not only found at a single point in the reciprocal space but were also measured in multiple Brillouin zones, as shown in Fig. 12 in Appendix A 2.

The appearance of additional peaks at the forbidden positions indicates that not only does the volume collapse below the transition, as shown in Fig. 7(c), but there is a possibility of the structure transforming to a different crystal symmetry from the high-temperature $P4/mmm$. Furthermore, peaks at $\tau = (0, 0, 0.5)$ and $(0.5, 0.5, 0.5)$ positions indicate the doubling of c as well as the enhanced in-plane unit-cell dimensions, with potentially $a' = b' = \sqrt{2}a$, similar to the DFT predictions in Sec. IV. Other possible scenarios, like $a' = b' = 2a$, can be ruled out because the observed feature in our $(H, 0, L)$ Bragg peaks is inconsistent with the lower crystal symmetry expected for this case. For instance, ISODISTORT [31] analysis of the potential subgroups, considering two \mathbf{k} -vectors $(0, 0, 0.5)$ and $(0.5, 0.5, 0.5)$ and their superposed irreducible representations (Irreps), suggests an orthorhombic crystal structure for $a' = b' = 2a$ and should lead to the splitting of the $(2, 0, 5)$ peak below transition, but no such splitting was observed in our data, as shown in Fig. 6. Additionally, in our measurements, we also checked for the splitting along the $[H, H, 0]$ direction by measuring $(1, 1, 6)$ Bragg peaks, and no such splitting was found. The results imply that the low-temperature crystal structure is potentially tetragonal because for other lower symmetry, splitting of the tetragonal Bragg peaks is expected due to the formation of the structural domains. Finally, since the satellite (superlattice) peaks were observed at two distinct and nonequivalent wave-vector positions, we categorized the low-temperature structure as double- Q structure with respect to room-temperature tetragonal $P4/mmm$.

Overall, our single-crystal x-ray diffraction measurements confirm that GaPt₅P undergoes a first-order structural transition from tetragonal $P4/mmm$ to a structure with potentially a different crystal symmetry, and with an enlarged unit cell of $a' = b' = \sqrt{2}a$ and $c' = 2c$. Additionally, the transition is characterized by the anisotropic changes of lattice parameters and a volume collapse with respect to the high-temperature tetragonal structure.

E. Transport under pressure in GaPt₅P: Enhancement of T_s towards room temperature

The apparent change in the unit-cell volume below the transition indicates that it should be possible to couple the transition to applied hydrostatic pressure. As a matter of fact, in a simplistic model, taking into account the volume collapse, hydrostatic pressure should enhance or promote the transition by driving T_s to the higher values. However, the anisotropic changes in the c and a lattice parameters allow for the possibility that this assumption might be oversimplified. Hence, to understand how the pressure affects the observed transition and to quantify its sensitivity, zero-field resistance measurements between 1.8 and 300 K were carried out on GaPt₅P single crystals at different pressures using a laboratory-made piston-cylinder pressure cell. The measurements, including the ambient pressure measurement outside the pressure cell,

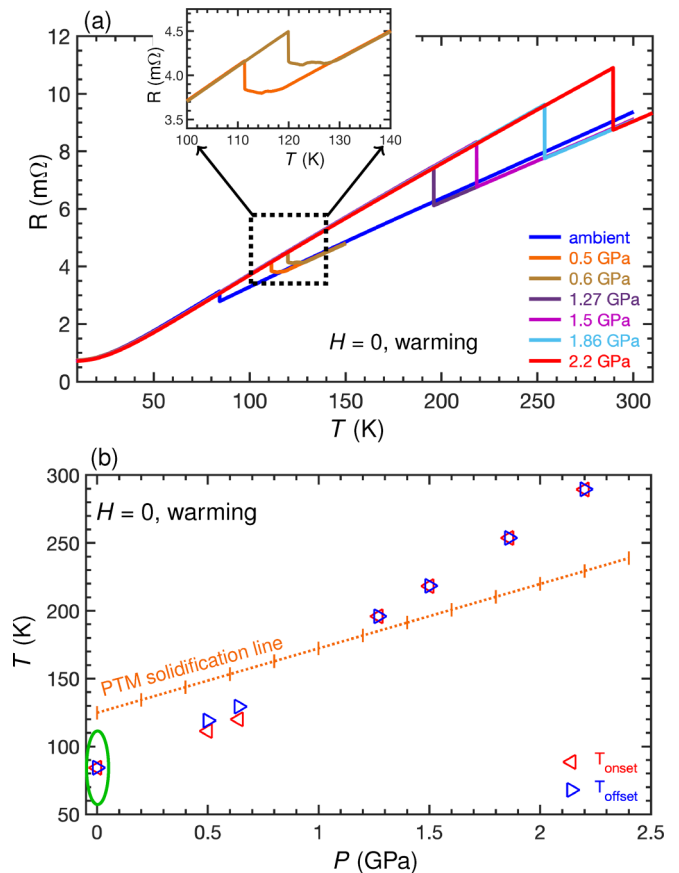


FIG. 9. (a) Temperature dependence measurements of the resistance at different pressures illustrating the increase in the feature (upturn or jump) corresponding to the structural transition. The inset is a magnified plot, zoomed in to highlight the broadening of an otherwise sharp upturn. (b) Pressure-temperature (P-T) phase diagram of GaPt₅P from $H = 0$ resistance measurements showing the onset and offset temperatures in (a). In addition, it contains the solidification line (dotted orange with vertical dashes) of the pressure-transmitting media (light oil and n -pentane) at different pressures taken from Ref. [17]. The green ellipse around the $P \sim 0$ GPa data is to emphasize that the ambient pressure measurements were done outside the pressure cell without any pressure media. A single crystal used for the pressure measurements, including ambient or zero pressure data, is different from the one used for Figs. 1 and 2, hence the ambient pressure data shown here are not the same as the data shown in those two figures.

were done on a single crystal different from the one used for the measurements in Figs. 1 and 2.

Figure 9(a), measured while warming, demonstrates the evolution of the in-plane resistance under pressure, revealing two distinct and noticeable features (similar plots of data taken upon cooling are shown in Fig. 13 in Appendix A 3 and demonstrate similar behavior). First, as expected, the transition temperature T_s increases with increasing pressure, reaching room temperature by 2.2 GPa. Second, in the intermediate pressure of $0 < P < 1.27$ GPa, the otherwise sharp steplike upturn broadens and contains multiple medium- and small-sized jumps. The zoomed-in figures in the upper inset, in Figs. 9(a) and 13(a), highlight the observed

broadening. Such broadening in resistance data is not uncommon in systems with anisotropic changes in the lattice parameters and transition temperature occurring below the solidification temperature of the pressure-transmitting media (PTM). In this scenario, the broadening is due to the nonhydrostatic conditions arising in the system. Broadened features in the resistance measurements under pressure due to nonhydrostaticity were also observed in LaSb₂, Ref. [32], where the pressure suppresses the charge-density-wave (CDW) transition. In this study, measurements were conducted using the same pressure cell and PTM as used for GaPt₅P. An extreme example of such solidified pressure-medium-induced broadening was observed in CaFe₂As₂ both in orthorhombic-antiferromagnetic and collapsed-tetragonal transitions when they occur below the PTM solidification line [33,34].

Figure 9(b), shown for warming, quantifies the broadening observed in GaPt₅P in a pressure range of $0 < P < 1.2$ GPa; the onset and offset (completion) temperatures of the transition are shown at each applied pressure up to 2.2 GPa along with the solidification line (SL) of the pressure medium (dotted orange with vertical dash) [17]. The P-T phase diagram can be divided into two regions separated by the PTM's SL: the region with $T_{\text{onset/offset}}$ above the solidification line and the one below the line. For transition temperatures above the SL (as well as for the ambient pressure data taken outside the pressure cell) the resistive transition feature is near vertical and the onset and offset temperatures are essentially identical, $\delta T = T_{\text{offset}} - T_{\text{onset}} \sim 0$, indicating a sharp and well-defined transition. For transition temperatures below the SL there is a clear difference ($\delta T > 0$) between onset and offset temperatures, thereby confirming and quantifying the broadening. The observed features indicate that the sharp (broadened) features in these measurements are dependent upon whether the transition temperature is above (below) the SL of the PTM, rather than the specific pressure values. Moreover, in GaPt₅P, unlike LaSb₂, an increase in pressure beyond 1.2 GPa, where the transition temperature is higher than the solidification temperature of PTM, leads to a sharpening of the transition feature akin to the measurement conducted at ambient pressure without the use of pressure media. In summary, the broadening arises due to the nonhydrostatic state in the sample resulting from the PTM solidification and anisotropic changes in the lattice parameters, and irrespective of the pressure values, it occurs exclusively when the transition temperature is lower than the solidification temperature of PTM.

In addition, the data in Fig. 9(b) allow us to quantify the sensitivity of GaPt₅P to hydrostatic pressure and make a comparative study with LaSb₂ [32], where the resistive features were found to be extremely sensitive to pressure with an overall pressure derivative of ~ -500 K/GPa. The moderately large slope $\frac{dT}{dP} \sim 100$ K/GPa for GaPt₅P, obtained from the blue and red data sets, indicates remarkable sensitivity to pressure and implies that the room-temperature crystal structure of GaPt₅P is quite fragile.

Additional notable findings are that, unlike in LaSb₂, there is almost no change in the width of thermal hysteresis except in the ill-defined broad nonhydrostatic regions. Similarly, in the hydrostatic region there was no significant change in the resistance jump $\frac{\delta\rho}{\rho}$, as shown in Fig. 14 below in Appendix A.3. Finally, small variation in $\frac{\delta\rho}{\rho}$ with pressure in

GaPt₅P implies that unlike LaSb₂, pressure drives the transition temperature to higher values in GaPt₅P without bringing any additional significant changes in the Fermi surface or electronic structure.

IV. DFT CALCULATIONS: PHONON SOFTENING

Among the members of the 1-5-1 family of compounds, the temperature-driven structural transition has been observed or reported exclusively in GaPt₅P. Given the similar structures reported for all 3A element ($X = \text{Al, Ga, In, Tl}$) $X\text{Pt}_5\text{P}$ members [7,10], one might reasonably expect similar physical behavior among all. However, our ambient pressure transport and magnetization measurements for AlPt₅P and InPt₅P, shown in Fig. 1, display metallic behavior and diamagnetism, respectively, without any features (anomalies) indicating the structural transition. From the viewpoint of the chemical pressure, one of our considerations was a possibility of the room-temperature structure being different from $P4/mmm$ in these compounds, especially in AlPt₅P with the smaller radius atom Al than Ga. However, refinements of our powder x-ray diffraction data, discussed in Sec. III C, confirm the structure of all three compounds to be $P4/mmm$.

Furthermore, no additional satellite peaks at $\tau = (0, 0, 0.5)$ and $(0.5, 0.5, 0.5)$ were observed on single-crystal x-ray diffraction measurements done on AlPt₅P. Similarly, only satellite peaks at $(0, 0, 0.5)$ positions were measured for InPt₅P and they were absent as well. This confirms that GaPt₅P is the sole member of the $X\text{Pt}_5\text{P}$ family where the structure transition occurs. Finally, it remains a challenge for computational studies to identify how and why the GaPt₅P compound is unique in this manner.

Considering the apparent uniqueness of GaPt₅P, other outstanding questions that remain are as follows: (i) what is the low-temperature crystal symmetry, and (ii) what drives the transition? Our DFT calculations provide some insights.

To investigate the structural transition of GaPt₅P, we carried out phonon calculations at 0 K with a finite displacement method in DFT. As shown in Figs. 10(a) and 10(c), the phonon band dispersion of the GaPt₅P primitive tetragonal structure in space group $P4/mmm$ (123) has an imaginary mode at the A point and around it along the R - A , A - Z , and M - A directions, which means the primitive tetragonal structure is dynamically unstable, agreeing with the experimental observation of the structural change on cooling. By following the eigenvector of the imaginary mode at the A point to double the unit cell vectors and after full relaxation, we find that the supercell of $(\sqrt{2} \times \sqrt{2} \times 2)$ rotated by 45° ($R45$) is energetically more stable by 30.5 meV/f.u. Interestingly, as shown in Fig. 10(b), the low-energy supercell structure seems to retain all the symmetries, hence it should belong to the tetragonal space group. Furthermore, in the structure, two out of every four Pt layers has a twist around the c -axis. The phonon band dispersion of the low-energy supercell structure in Fig. 10(d) now shows dynamical stability with no imaginary phonon modes, hence the low-energy supercell structure of $(\sqrt{2} \times \sqrt{2} \times 2)R45$ with lattice parameters $a' = b' = \sqrt{2}a$ and $c' = 2c$ is likely the low-temperature structure. Nevertheless, the experimental determination and confirmation of the crystal structure symmetry at low temperatures are still pending.

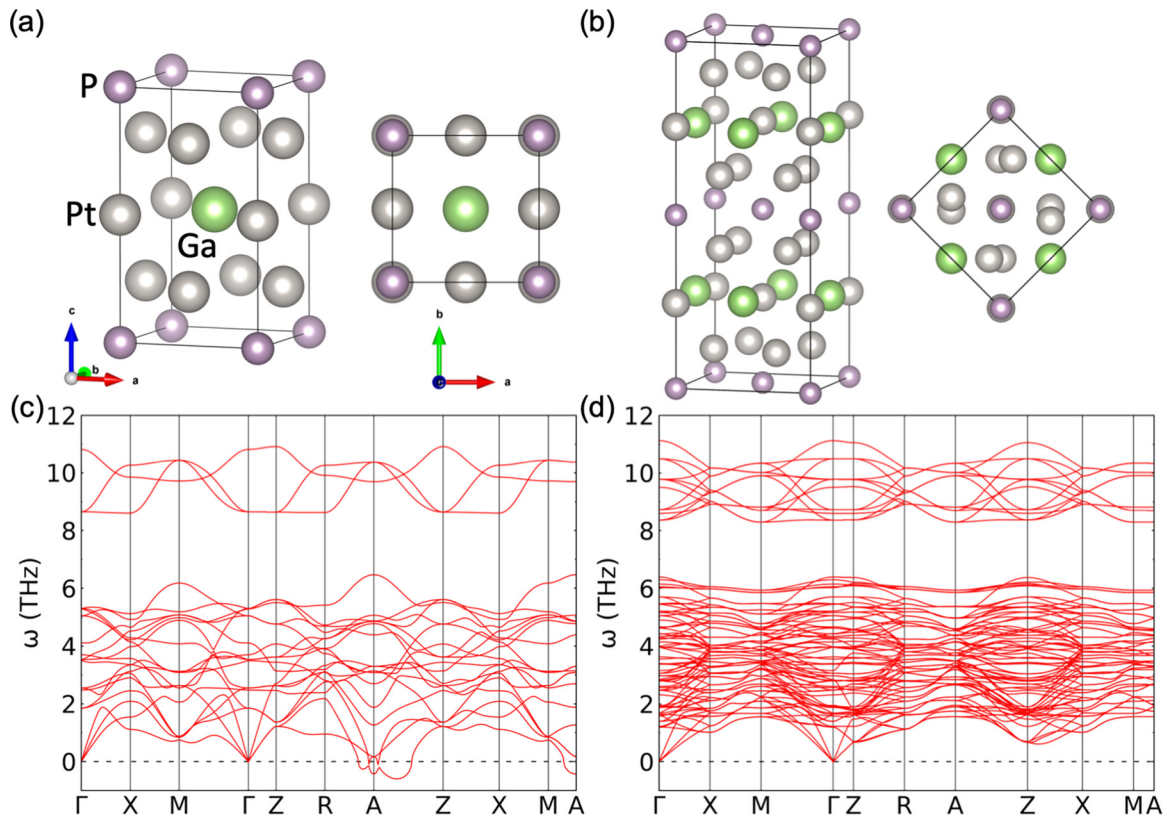


FIG. 10. Crystal structures and phonon band dispersions of GaPt_5P from the 0 K DFT calculations. Side-view and top-view along the c -axis of (a) high- T primitive tetragonal structure in space group $P4/mmm$ (123), and (b) low-energy structure of $(\sqrt{2} \times \sqrt{2} \times 2)R45$ supercell. Phonon band dispersion of (c) high- T primitive tetragonal structure and (d) low-energy structure of $(\sqrt{2} \times \sqrt{2} \times 2)R45$ supercell.

Similar phonon calculations done on two other members AlPt_5P and InPt_5P lack imaginary modes in their phonon band dispersion, as shown in Fig. 16 in Appendix A 5. The results agree with the experimental observation of no structural changes in these compounds, and they reemphasize the association of the imaginary modes with the structural transition in GaPt_5P .

To summarize, our DFT calculations suggest a potential low-temperature structure and identify softening of phonons as a driving mechanism for the transition. However, this likely captures only a partial aspect of the observed phenomena in GaPt_5P . First, these calculations only account for the presence of superlattice peaks at wave-vector positions $(0.5, 0.5, 0.5)$, leaving the origin of the $(0, 0, 0.5)$ superlattice peaks unexplained. Also, the soft modes are generally invoked for a second-order phase transition [35,36], unlike the first-order transition observed in GaPt_5P . As a result, the origin of these $(0, 0, 0.5)$ superlattice peaks and the underlying reason for the system's double- Q type structural transition remain unanswered questions. An explanation for the unexplained $(0, 0, 0.5)$ superlattice peaks could be that they are charge density wave (CDW) peaks associated with the underlying charge modulation and structural transition having an electronic origin. However, the hypothesis remains open for future investigations. Given that CDW may arise from Fermi surface nesting, our DFT calculations explored hints of nesting corresponding to the superlattice wave vectors but did not find any definitive evidence.

Further experimental and computational investigations are necessary to resolve the ambiguity, completely understand the microscopic mechanisms behind the transition, and identify the uniqueness of GaPt_5P that leads to the structural transition. The first step in that direction is to unambiguously determine the low-temperature crystal structure, and the refinement of the low-temperature single-crystal x-ray diffraction data would be the appropriate method to achieve this goal. Also, the inelastic x-ray or neutron scattering measurements of phonons with temperature can help to confirm and rule out the softening of phonons at $(0.5, 0.5, 0.5)$ and $(0, 0, 0.5)$ wave-vector positions, respectively.

V. SUMMARY

In summary, characterization of single crystals of $X\text{Pt}_5\text{P}$ ($X = \text{Al}, \text{Ga}, \text{In}$) using various techniques, such as transport, magnetization, and single-crystal and powder x-ray diffraction measurements, revealed that GaPt_5P exhibits anomalous behavior at low-temperature (~ 80 K) corresponding to a structural transition. No such features were present in AlPt_5P and InPt_5P in the temperature range of 2–300 K. Furthermore, the structural transition in GaPt_5P is first order, and is characterized by anisotropic changes in the lattice parameters and volume collapse. Among the members of the 1-5-1 family, GaPt_5P stands alone in exhibiting the structural transition. The underlying reason for the unique behavior in GaPt_5P remains to be understood, but our DFT calculations offer some insights

by suggesting that phonon softening could potentially be one of the mechanisms for the transition.

Additionally, the pressure-dependent measurements of the resistive features indicate that GaPt₅P is remarkably sensitive to pressure, and the room-temperature tetragonal $P4/mmm$ structure is fragile. Also, there were noticeable experimental artifacts, such as smeared and broadened transitions, which can be attributed to the nonhydrostatic conditions occurring below the solidification line of the PTM, and irrespective of the pressure values, they occur exclusively when the transition temperature is lower than the solidification temperature of PTM.

ACKNOWLEDGMENTS

Work at Ames National Laboratory was supported by the U.S. Department of Energy (DOE), Basic Energy Sciences, Division of Materials Sciences & Engineering, under Contract No. DE-AC02-07CH11358. Use of the Advanced Photon Source at Argonne National Laboratory was supported by the U.S. Department of Energy, Office of Science, Office of Basic Energy Sciences, under Contract No. DE-AC02-06CH11357.

APPENDIX

1. Density Functional Theory Calculations

Electronic structures of GaPt₅P from the DFT calculations are shown in Fig. 11, and features consistent with the 3D metallic behavior are apparent. In (a), band dispersion crossing the Fermi level along all directions except for $X-M$ and $R-A$ is clearly observed, and in (b) a small but non-negligible Pt 5d density of states at E_F exists. The small density of states near the Fermi level is consistent with the observed diamagnetism.

2. Superlattice peaks in different Brillouin zones

Figure 12 shows $\tau = (0, 0, 0.5)$ -type superlattice peaks in different Brillouin zones.

3. Additional pressure dependence of the resistance features

Figure 13(a) demonstrates the evolution of the in-plane resistance under pressure data, which were measured while cooling, and similar to the warming [Fig. 9(a) in the main

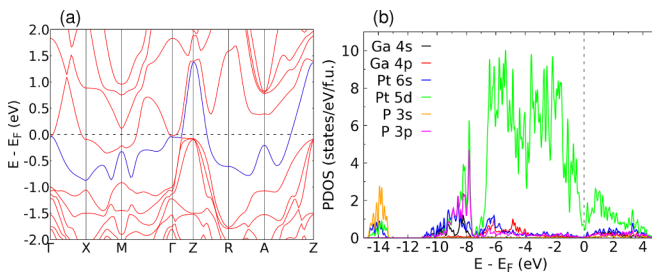


FIG. 11. (a) Band structures and (b) partial density of states for GaPt₅P from DFT calculations, corresponding to high-temperature tetragonal $P4/mmm$ structure. The blue line in (a) represents the top valence band according to simple band filling to distinguish the hole and electron pockets.

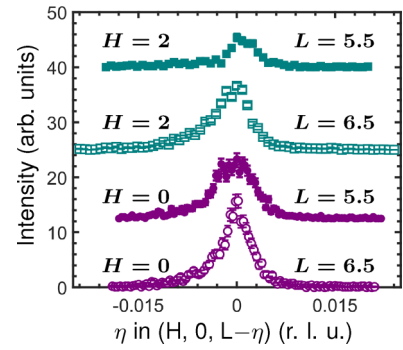


FIG. 12. $[0, 0, L]$ scans of the half-integer L peaks at $T = 13$ K for $H = 0$ and 2.

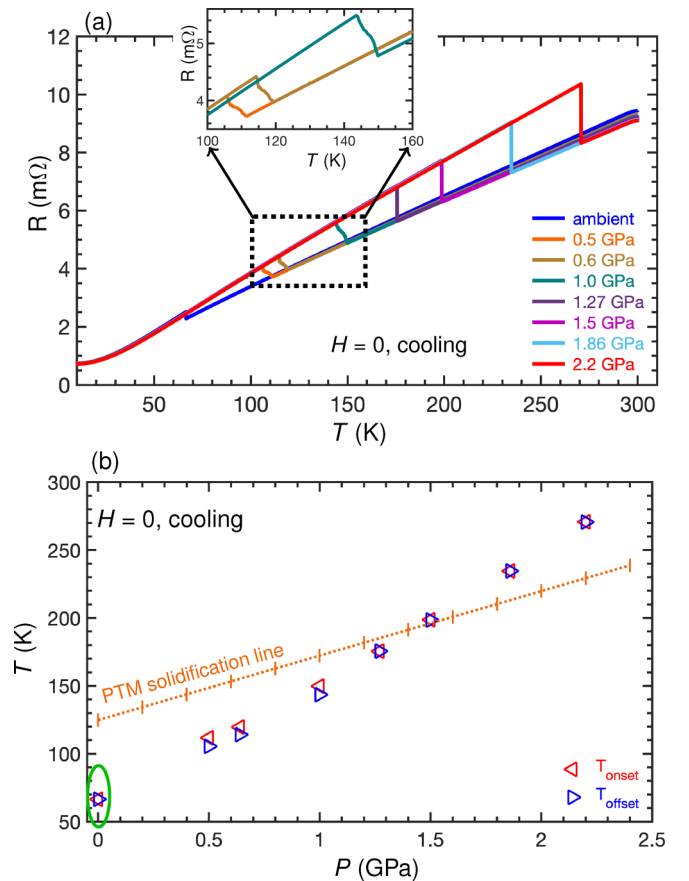


FIG. 13. (a) Temperature dependence measurements of the resistance at different pressures illustrating the increase in the feature (upturn or jump) corresponding to the structural transition. Upper inset is a magnified plot, zoomed in to highlight the broadening of an otherwise sharp upturn. (b) Pressure-temperature (P - T) phase diagram of GaPt₅P from $H = 0$ resistance measurements showing the onset and offset temperatures in (a). In addition, it contains a solidification line (dotted orange with vertical dashes) of the pressure-transmitting media (light oil and n -pentane) at different pressures [17]. The green ellipse around the $P \sim 0$ GPa data is to emphasize that the ambient pressure measurements were done outside the pressure cell without any pressure media. A single crystal used for the measurements is different from the one used for Figs. 1 and 2.

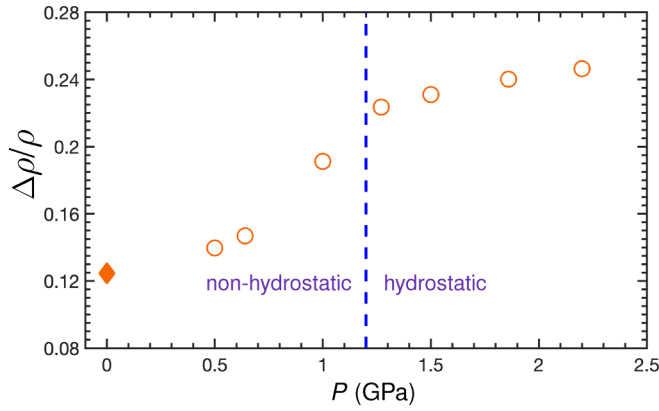


FIG. 14. Relative size, $\Delta\rho/\rho$, of the feature in resistance (resistivity) as a function of pressure. The blue dashed line indicates the pressure below which the PTM solidifies and nonhydrostatic conditions are met. The filled diamonds correspond to the ambient pressure measurements outside the pressure cell.

text], it demonstrates two distinct and noticeable features: (i) enhancement of the transition temperature T_s with increasing pressure, and (ii) multiple medium and small sized jumps for the pressure $0 < P < 1.27$ GPa. The P-T phase diagram in Fig. 13(b) reconfirms and quantifies the broadening ($\delta T > 0$) for these pressure values and illustrates that both the onset and offset transitions occur below the solidification lines of PTM.

$\Delta\rho/\rho$ in Fig. 14 was obtained by a methodology similar to that used in Ref. [32]. Its value nearly doubles (to a 24% increase) by 2.2 GPa, but change is very small in comparison to LaSb_2 , where it increases to 1 (100% increase) on increasing pressure to ~ 0.2 GPa. Moreover, in LaSb_2 the value decreases abruptly in the nonhydrostatic region and eventually disappears. However, no such behavior occurs in GaPt_5P except for the slight deviations with a small decrease below 1.27 GPa in the nonhydrostatic region. Nevertheless, the small and decreased value of $\Delta\rho/\rho$ for the ambient pressure measurement in the figure prevents it from making a clear correlation between the decrease and nonhydrostaticity.

Also, the 100% increase in LaSb_2 in the hydrostatic region was associated with the further gapping of the Fermi surface [32]. Similarly, only a small variation in $\Delta\rho/\rho$ in GaPt_5P up to 2.2 GPa implies that pressure on GaPt_5P brought no additional significant changes in the Fermi surface or electronic structure.

4. History and ramp-rate dependence of the hysteresis width and transition temperature

Figure 15 shows the magnetization measurements done on a cluster of GaPt_5P single crystals, and the measurements were done using a VSM option of the MPMS3 with continuous temperature sweeps. Figure 15(a) illustrates that both the hysteresis width and the transition temperatures (onset or offset) vary for the measurement done with different cooling (warming) rates. Similarly, Fig. 15(b) demonstrates that the variation also occurs for the measurements with the same ramp-rate but with different thermal history. Hence, the first-order transition of GaPt_5P exhibits a history dependence, and this is one of the possible reasons why the different

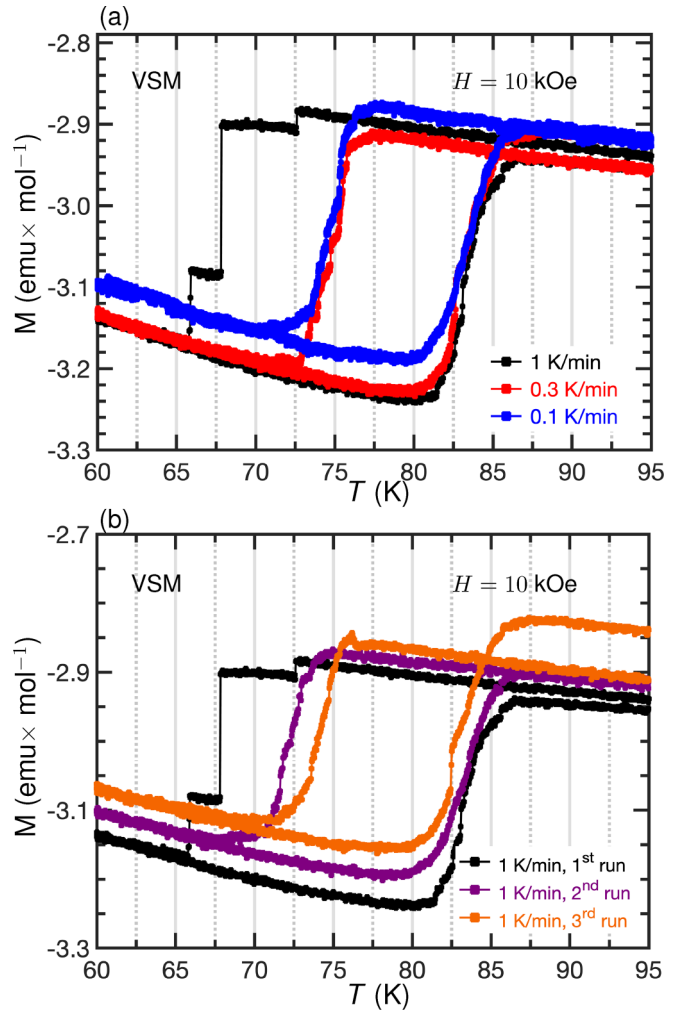


FIG. 15. Magnetization measurements done on a cluster of GaPt_5P single crystals using a VSM option of the MPMS3 with continuous temperature sweeps and field $H = 10$ kOe. The figures illustrate variation in the hysteresis width and transition temperature for measurements done with (a) different ramp-rates and (b) different cycles with a ramp-rate of 1 K/min. In (b) the first run was the first measurement that started from the room temperature, the second run followed it with the measurement up to 180 K, and the third run was measured after leaving the cluster at 180 K for several hours.

measurements discussed above in the main text exhibit slight variations in the hysteresis width and transition temperatures.

5. Phonon band dispersions for AlPt_5P and InPt_5P

Figure 16 shows phonon dispersions, from 0 K DFT calculations, for all three members: (a) AlPt_5P , (b) GaPt_5P , and (c) InPt_5P . The calculations are done for the high- T primitive tetragonal structure of each compound with their relaxed lattice parameters. The figures clearly show that the imaginary modes in GaPt_5P at the A point and around it along the R - A , A - Z , and M - A directions are absent in both AlPt_5P and InPt_5P . The absence of any imaginary modes in their (AlPt_5P and InPt_5P) phonon dispersion is consistent with the experimental results of no structural transition in these two

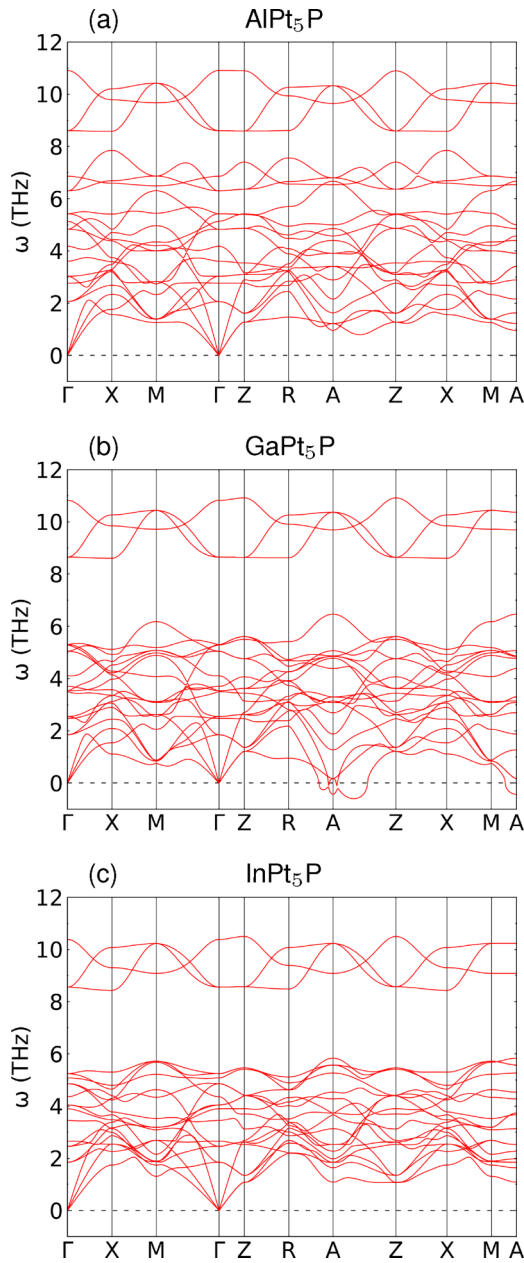


FIG. 16. Phonon band dispersion, at 0 K, of high- T primitive tetragonal structure of all three members, (a) AlPt₅P, (b) GaPt₅P, and (c) InPt₅P.

members. Hence, the imaginary mode related to the lattice instability is the unique feature of GaPt₅P among all reported 1-5-1 compounds.

6. Effects of Al and In substitution in GaPt₅P

The high-pressure resistance measurements show that applying hydrostatic pressure to GaPt₅P rapidly enhances the temperature at which the structural phase transition occurs. With this in mind, we were interested to also explore the effect of chemical substitution by alloying GaPt₅P with the smaller Al atoms, i.e., Ga_{1-x}Al_xPt₅P, hoping that this would induce the positive chemical pressure, thereby allowing us to push the transition to higher temperature for a more convenient

TABLE IV. In fraction in Ga_{1-x}In_xPt₅P estimated from the EDS measurements.

Nominal x	EDS x				Average
	Spot 1	Spot 2	Spot 3	Spot 4	
0.025	0.0724	0.0451	0.0323	0.0295	0.04(2)
0.05	0.0597	0.0886	0.08027	0.09162	0.08(1)

study at ambient pressures. Likewise, we also attempt to do the opposite and study the effect of negative chemical pressure by alloying with the larger In atoms, Ga_{1-x}In_xPt₅P.

Single crystals of Al and In substituted GaPt₅P were grown in the same manner as the pure GaPt₅P discussed in the main text but with starting nominal compositions of (Ga_{1-x}A_x)₉Pt₇₁P₂₀ for A = Al and In and $x = 0.025$ and 0.05 . The heating, cooling, and decanting conditions were otherwise identical to the protocol outlined in the crystal growth section in the main text. EDS measurements were carried out to determine the Al and In levels in the final crystals, and the pure AlPt₅P, GaPt₅P, and InPt₅P were used as standards.

Table IV shows the results of EDS measurements on the In alloyed Ga_{1-x}In_xPt₅P. To assess the sample homogeneity, four measurements were made on different spots on the sample surfaces, and we use the average values of each as the measured x in the following discussion. The uncertainties are the standard deviations of the four x values measured for each sample. The EDS measurements show that the measured fraction of In is slightly higher than the nominal values, but that an increasing quantity of In is substituted for Ga as the nominal x increases. In the case of the Al-alloyed samples, we were unable to quantify the alloy fraction of Al, as the measured Al quantity was smaller than the uncertainty in our measurements for both nominally $x = 0.025$ and 0.05 samples. Therefore, for Ga_{1-x}Al_xPt₅P, we only refer to the nominal x values in the following discussion to distinguish between samples.

Figure 17 shows the powder x-ray diffraction patterns for In and Al alloyed GaPt₅P. The measurements were done using our in-house x-ray unit, Rigaku Miniflex-II instrument operating with Cu $K\alpha$ radiation, $\lambda = 1.5406 \text{ \AA}$ ($K_{\alpha 1}$) and 1.5443 \AA ($K_{\alpha 2}$), at 30 kV and 15 mA. In each pattern, the most intense reflections are in good agreement with the expected peaks for the $P4/mmm$ structure of GaPt₅P. Several patterns also show a few much weaker reflections that can be indexed to PtP₂. The lattice constants refined from the above powder patterns are shown in Figs. 18(a)–18(c) for In alloyed samples and in 18(d)–18(f) for Al alloyed samples. The lattice parameters of the Ga_{1-x}In_xPt₅P samples behave as expected, as a , c , and the unit-cell volume V all increase in a nearly linear manner as the measured In fraction is raised, consistent with the larger radius of In compared to Ga. This result is consistent with the EDS data and suggests a steady increase in In as the nominal x is raised.

In the case of Ga_{1-x}Al_xPt₅P, we can only compare the measured lattice parameters with the nominal fraction of Al added to the initial growth compositions. We find that for Ga_{1-x}Al_xPt₅P, the a lattice parameter does not show a uniform trend with nominal doping and increases slightly at low x , but

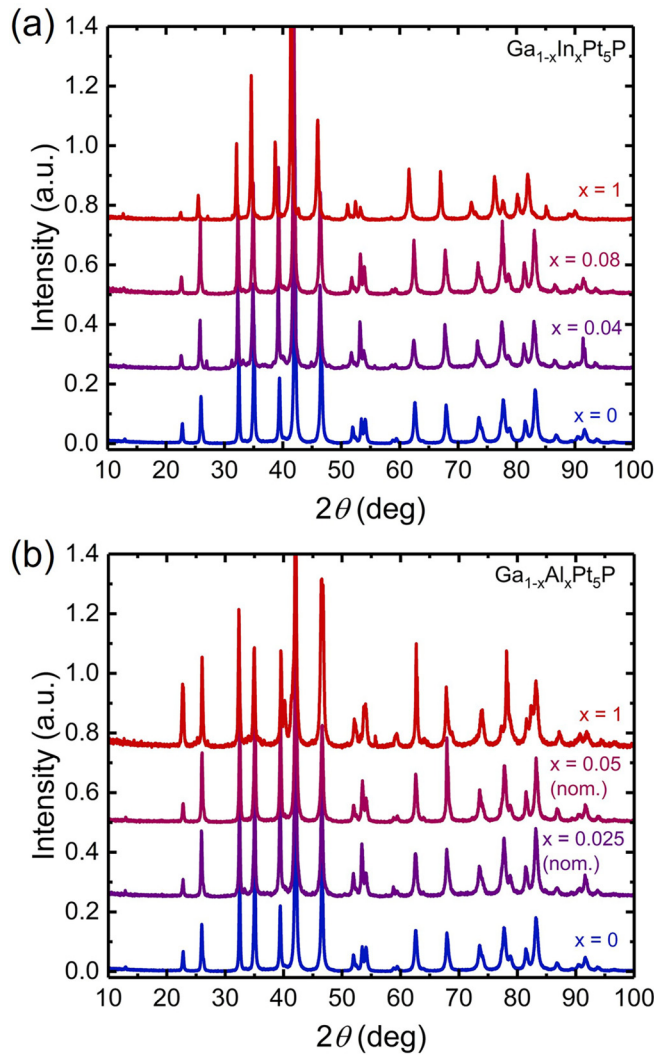


FIG. 17. (a) and (b) Powder x-ray diffraction patterns for $\text{Ga}_{1-x}\text{In}_x\text{Pt}_5\text{P}$ and $\text{Ga}_{1-x}\text{Al}_x\text{Pt}_5\text{P}$, respectively.

shrinks to ~ 3.896 Å for AlPt_5P . While the initial increase in a at low nominal x appears anomalous, the overall decrease of a from pure GaPt_5P to AlPt_5P is only $\sim 0.01\%$, meaning that the a lattice parameter is effectively insensitive to Al substitution. On the other hand, c and unit-cell volume both decrease by about 1% moving from GaPt_5P to AlPt_5P . The changes in the lattice parameters and volume from GaPt_5P to AlPt_5P are similar to the synchrotron measurement results, listed in Table III.

To determine the evolution of the structural transition in the alloyed samples, we measured the temperature dependence of the resistance, and the results are shown in Figs. 19(a) and 19(b) for In and Al alloyed samples, respectively. In both cases, the structural transition is suppressed quickly upon substitution of Ga. The transition is completely absent in both $x = 0.04$ and 0.08 $\text{Ga}_{1-x}\text{In}_x\text{Pt}_5\text{P}$ samples. In the Al-doped samples, we find the transition is subtly suppressed from 72 K (on cooling) or 84 K (on warming) in pure GaPt_5P to 66 K (on cooling) or 77 K (on warming) for nominally $x = 0.025$, and it vanishes by nominally $x = 0.05$. We note here that despite being unable to resolve the Al fraction with

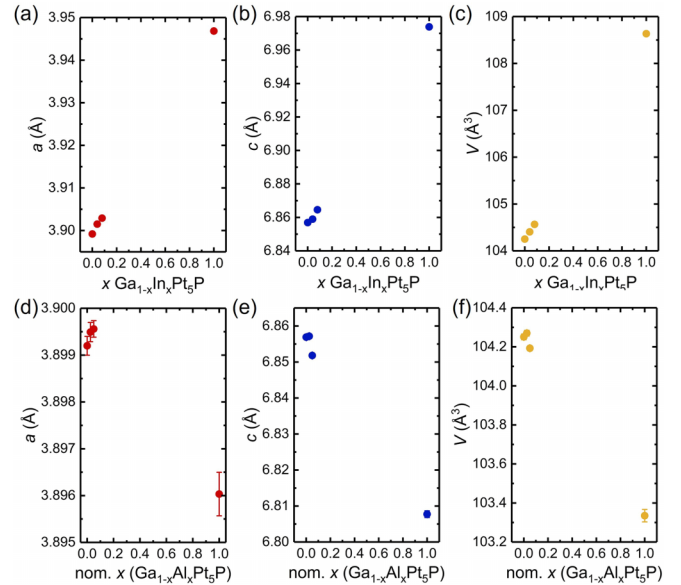


FIG. 18. Dependence of the a and c lattice parameters and volume with In composition in $\text{Ga}_{1-x}\text{In}_x\text{Pt}_5\text{P}$ (a)–(c) and Al composition in $\text{Ga}_{1-x}\text{Al}_x\text{Pt}_5\text{P}$ (d)–(f). X corresponds to EDS results for $\text{Ga}_{1-x}\text{In}_x\text{Pt}_5\text{P}$ and nominal concentration for $\text{Ga}_{1-x}\text{Al}_x\text{Pt}_5\text{P}$.

our EDS measurements, the fact that the structure change is clearly suppressed and eliminated for nominally $x = 0.025$ and 0.05 $\text{Ga}_{1-x}\text{Al}_x\text{Pt}_5\text{P}$ indicates a possibility of a small but finite quantity of Al replacing Ga.

Considering the high-pressure data, these results are surprising. Because application of hydrostatic pressure rapidly increases the transition temperature, we anticipated the smaller Al atoms would provide “positive chemical pressure” and also raise the transition temperature, and the larger In atoms would do the opposite. The data obtained for the In alloyed samples superficially agree with this prediction. However, given that 4% In leads to a $\sim 0.17\%$ volume increase and eliminates the transition, the rate at which the transition

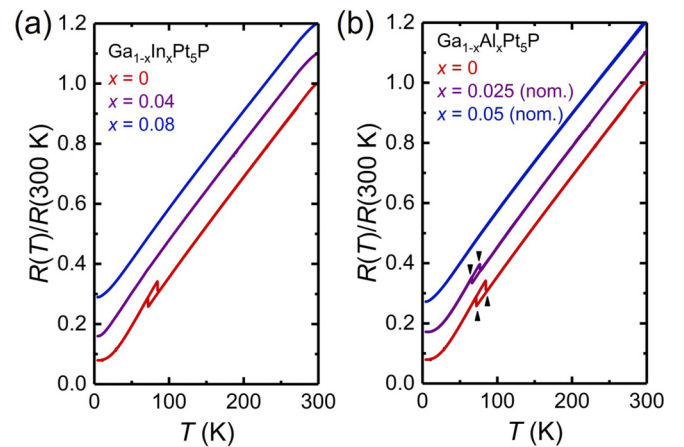


FIG. 19. Temperature dependence of $R(T)/R(300\text{ K})$ for three different In (a) and Al (b) concentrations, illustrating the rapid suppression of the transition feature with substitution. The Al levels indicated in the figures are the nominal concentration.

vanishes is considerably faster than expected based on “negative chemical pressure” alone. In fact, it is at least twice as fast when considering $\sim 0.33\%$ volume change below the transition, shown in Fig. 7(c). On the other hand, Fig. 18(c) shows that the overall unit-cell volume of GaPt₅P is effectively unchanged by small Al substitution (less than 0.1% at nominally $x = 0.05$), but the structural transition is rapidly suppressed and eliminated in Ga_{1-x}Al_xPt₅P. Taken together, the data in Fig. 19 indicate (i) that the structural transition in GaPt₅P is extraordinarily fragile and can be eliminated with

even a relatively gentle perturbation of dilute chemical substitution, and (ii) chemical substitution likely has a different effect from applied pressure, and “chemical pressure” is not the correct framework with which to understand the effect of substitution. One possibility is that GaPt₅P is very sensitive to disorder, but we do not at present understand the nature of the extreme sensitivity of the transition. Ultimately, more detailed doping and alloying studies beyond the scope of this work are needed to understand the response of GaPt₅P to external tuning parameters.

-
- [1] X. Gui and W. Xie, *Chem. Mater.* **32**, 3922 (2020).
- [2] X. Gui, R. A. Klein, C. M. Brown, and W. Xie, *Inorg. Chem.* **60**, 87 (2021).
- [3] R. S. Dissanayaka Mudiyansele, Q. Zhang, M. Marshall, M. Croft, Z. Shu, T. Kong, and W. Xie, *Inorg. Chem.* **61**, 3981 (2022).
- [4] T. J. Slade and P. C. Canfield, *Z. Anorg. Allg. Chem.* **648**, e202200145 (2022).
- [5] T. J. Slade, N. Furukawa, T. R. Smith, J. Schmidt, R. S. D. Mudiyansele, L.-L. Wang, W. Xie, S. L. Bud'ko, and P. C. Canfield, *Phys. Rev. Mater.* **7**, 024410 (2023).
- [6] T. J. Slade, R. S. D. Mudiyansele, N. Furukawa, T. R. Smith, J. Schmidt, L.-L. Wang, C.-J. Kang, K. Wei, Z. Shu, T. Kong, R. Baumbach, G. Kotliar, S. L. Bud'ko, W. Xie, and P. C. Canfield, *Phys. Rev. B* **107**, 134429 (2023).
- [7] M. El-Boragy and K. Schubert, *Int. J. Mater. Res.* **61**, 579 (1970).
- [8] X. Gui, M. Marshall, R. S. Dissanayaka Mudiyansele, R. A. Klein, Q. Chen, Q. Zhang, W. Shelton, H. Zhou, C. M. Brown, H. Cao, M. Greenblatt, and W. Xie, *ACS Appl. Electron. Mater.* **3**, 3501 (2021).
- [9] M. Fujioka, M. Ishimaru, T. Shibuya, Y. Kamihara, C. Tabata, H. Amitsuka, A. Miura, M. Tanaka, Y. Takano, H. Kaiju, and J. Nishii, *J. Am. Chem. Soc.* **138**, 9927 (2016).
- [10] E. Y. Zakharova, S. M. Kazakov, A. Götze, H. Kohlmann, and A. N. Kuznetsov, *J. Solid State Chem.* **265**, 266 (2018).
- [11] Canfield Crucible Sets, <https://www.lspceramics.com/canfield-crucible-sets-2/>, [Accessed: 22-December-2022].
- [12] P. C. Canfield, T. Kong, U. S. Kaluarachchi, and N. H. Jo, *Philos. Mag.* **96**, 84 (2016).
- [13] P. C. Canfield, *Rep. Prog. Phys.* **83**, 016501 (2020).
- [14] B. H. Toby and R. B. Von Dreele, *J. Appl. Crystallogr.* **46**, 544 (2013).
- [15] S. L. Bud'ko, A. N. Voronovskii, A. G. Gapotchenko, and E. S. Itskevich, *Zh. Eksp. Teor. Fiz.* **86**, 778 (1984).
- [16] A. Eiling and J. S. Schilling, *J. Phys. F* **11**, 623 (1981).
- [17] M. S. Torikachvili, S. K. Kim, E. Colombier, S. L. Bud'ko, and P. C. Canfield, *Rev. Sci. Instrum.* **86**, 123904 (2015).
- [18] P. Hohenberg and W. Kohn, *Phys. Rev.* **136**, B864 (1964).
- [19] W. Kohn and L. J. Sham, *Phys. Rev.* **140**, A1133 (1965).
- [20] P. E. Blöchl, *Phys. Rev. B* **50**, 17953 (1994).
- [21] G. Kresse and J. Furthmüller, *Phys. Rev. B* **54**, 11169 (1996).
- [22] G. Kresse and J. Furthmüller, *Comput. Mater. Sci.* **6**, 15 (1996).
- [23] H. J. Monkhorst and J. D. Pack, *Phys. Rev. B* **13**, 5188 (1976).
- [24] A. Togo and I. Tanaka, *Scr. Mater.* **108**, 1 (2015).
- [25] S. Mugiraneza and A. M. Hallas, *Commun. Phys.* **5**, 95 (2022).
- [26] S. Fan, L. Yang, and G. Gao, *Phys. Lett. A* **383**, 3138 (2019).
- [27] W. E. Haynes, *CRC Handbook of Chemistry and Physics* (CRC, Boca Raton, FL, 2016).
- [28] T. Sahu, *Phys. Rev. B* **43**, 2415 (1991).
- [29] P. J. Dean, D. Bimberg, and F. Mansfield, *Phys. Rev. B* **15**, 3906 (1977).
- [30] A. Baghdadi, A. Finley, P. Russo, R. J. Arnott, and A. Wold, *J. Less-Common Met.* **34**, 31 (1974).
- [31] B. J. Campbell, H. T. Stokes, D. E. Tanner, and D. M. Hatch, *J. Appl. Crystallogr.* **39**, 607 (2006).
- [32] S. L. Bud'ko, S. Huyan, P. Herrera-Siklody, and P. C. Canfield, *Philos. Mag.* **103**, 561 (2023).
- [33] M. S. Torikachvili, S. L. Bud'ko, N. Ni, and P. C. Canfield, *Phys. Rev. Lett.* **101**, 057006 (2008).
- [34] P. C. Canfield, S. L. Bud'ko, N. Ni, A. Kreyssig, A. I. Goldman, R. J. McQueeney, M. S. Torikachvili, D. N. Argyriou, G. Luke, and W. Yu, *Physica C* **469**, 404 (2009).
- [35] R. Cowley, *Adv. Phys.* **29**, 1 (1980).
- [36] J. Krumhansl, *Solid State Commun.* **84**, 251 (1992).